JGR Space Physics

RESEARCH ARTICLE
10.1029/2023JA031476

Secondary Gravity Waves From the Tonga Volcano Eruption: Observation and Modeling Over New Zealand and Australia

C. A. O. B. Figueiredo[1], S. L. Vadas[2], E. Becker[2], C. M. Wrasse[1], H. Takahashi[1], P. K. Nyassor[1], and D. Barros[1]

[1]Space Weather Division, National Institute for Space Research (INPE), São José dos Campos, Brazil, [2]Northwest Research Associates, EUA, Boulder, CO, USA

Key Points:

- The first TIDs observed over New Zealand and Australia originate at $z > 160$ and $z > 100$ km about 436 km southeast of the eruption
- This location agrees with model results for the body force created by the dissipation of primary GWs from the eruption
- The first TIDs observed over New Zealand and Australia are secondary, not primary, gravity waves from the eruption

Supporting Information:

Supporting Information may be found in the online version of this article.

Correspondence to:

C. A. O. B. Figueiredo and S. L. Vadas, anagetinga@gmail.com; cosme.figueiredo@inpe.br; vasha@nwra.com

Citation:

Figueiredo, C. A. O. B., Vadas, S. L., Becker, E., Wrasse, C. M., Takahashi, H., Nyassor, P. K., & Barros, D. (2023). Secondary gravity waves from the Tonga volcano eruption: Observation and modeling over New Zealand and Australia. *Journal of Geophysical Research: Space Physics*, *128*, e2023JA031476. https://doi.org/10.1029/2023JA031476

Received 10 MAR 2023
Accepted 7 OCT 2023

Abstract The biggest volcanic eruption since 1991 happened on 15 January 2022 on the island of Hunga Tonga-Hunga Ha'apai (20.6°S; 175.4°W) in the South Pacific between 4:00 and 4:16 UT. The updrafts from the eruption reached 58 km height. In order to observe its ionospheric effects, approximately 750 GNSS receivers in New Zealand and Australia were used to calculate the detrended total electron content (dTEC). Traveling ionospheric disturbances (TIDs) were observed over New Zealand 1.0–1.5 hr after the volcano eruption, with a horizontal wavelength (λ_H) of 1,525 km, horizontal phase velocity (C_H) of 635 m/s, period (τ) of 40 min, and azimuth (α) of 214°. On the other hand, TIDs were observed 2–3 hr after the eruption in Australia with λ_H, C_H, τ, and α of 922 km, 375 m/s, 41 min, and 266°, respectively. Using reverse ray tracing, we found that these GWs originated at $z > 100$ km at a location ~500 km south of Tonga, in agreement with model results for the location of a large amplitude body force created from the breaking of primary GWs from the eruption. Thus, we found that these fast GWs were secondary, not primary GWs from the Tonga eruption.

1. Introduction

On 15 January 2022, between 4:00 and 4:16 UT a major volcanic eruption occurred on the island of Hunga Tonga-Hunga Ha'apai (20.6°S; 175.4°W) (hereafter "Tonga") in the South Pacific (bib_gusman_and_roger_2022Gusman & Roger, 2022; Poli & Shapiro, 2022). This volcanic eruption occurred below the ocean surface. The water in contact with the magma quickly turned into gas that expanded rapidly and reached very high altitudes (Wright et al., 2022). The explosion reached a magnitude of 9–37 Mtons of TNT (Astafyeva et al., 2022) which corresponds to 600–2,000 times more energy than the Hiroshima and Nagasaki atomic bombs (15ktons of TNT). According to NASA researchers using data from Geostationary satellites GOES-17 and Himawari-8, the volcanic plume reached approximately 58 km, which is the highest altitude ever recorded by this type of phenomenon (Carr et al., 2022).

A volcanic eruption generates acoustic and gravity waves that propagate upward into the atmosphere. These waves are called co-volcanic ionospheric disturbances (CVIDs) when they reach the ionosphere. The timing of CVIDs in the ionosphere can vary based on the observer's location and the epicenter. Also, they have been observed directly above the volcano as far as 800–1,000 km and propagate at speeds of between 550 and 1,100 m/s (e.g., Astafyeva, 2019).

The eruption of Mount Pinatubo on 15 June 1991 caused ionospheric disturbances over Japan, as reported by IGAKASHI et al.(1993). The authors used 15-MHz HF Doppler and total electron content data to detect traveling ionospheric disturbances (TIDs) with a period of 12–21 min and a speed of 290 m/s. On the other hand, after the Tonga volcano eruption, Themens et al. (2022) observed large-scale TIDs (LSTIDs) propagating radially outward from the Tonga volcano with radial speeds of 200–950 m/s over New Zealand, Australia, Japan, Hawaii, Northeastern America, South Africa, and Northern Europe. In addition, Lin et al. (2022) observed TIDs over New Zealand (~5:00 UT) and Australia (~06:30 UT) and conjugate TIDs in the northern hemisphere due to TIDs from Australia. Zhang et al. (2022) observed LSTIDs (600–1,000 m/s) and medium-scale TIDs (300–350 m/s) around the world due to Tonga's volcanic eruption.

Vadas et al. (2023b) presented a comparison of observed and model results for MSTIDs and LSTIDs on a global scale. The study found that the fastest LSTIDs reached the regions of the US and South America at around 8:30–9:00 UT. These waves have a horizontal phase speed of 680 m/s, a horizontal wavelength of 3,400 km, and a period of 83 min. These values are consistent with the model results. On the other hand, the present

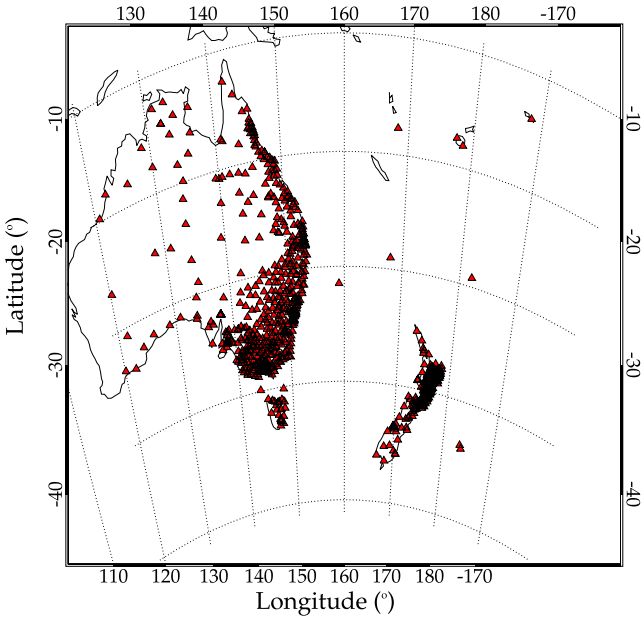

Figure 1. GNSS receivers in Australia and New Zealand during the Tonga volcanic eruption on 15 January 2022 from which the dTEC calculated.

study focuses on the physical mechanism that generated the TIDs observed over New Zealand and Australia from the Tonga eruption. We extract the parameters of the first TIDs from detrended TEC maps. Next, we use the reverse ray tracing model to determine if these waves could be primary or secondary gravity waves. Then, we discuss the results from The Model for gravity wavE SOurce. Ray trAcing and reConstruction (MESORAC) and the HIgh Altitude Mechanistic general Circulation Model (HIAMCM), which model the primary and secondary GWs created from the volcanic eruption. Finally, we compare the observed TIDs with the SAMI 3 and the other model results and determine the source of these observed TIDs over New Zealand and Australia.

2. Instrumentation and Methodology

2.1. Detrend TEC Maps

In order to observe the wave signatures from the Tonga eruption in the ionosphere, we use GNSS receivers to calculate the TEC. Figure 1 shows the locations of about 750 GNSS receivers (red triangles) in New Zealand and Australia on 15 January 2022. We calculated the vertical TEC (VTEC) from GPS and GLONASS constellations every 30 s. We calculated the dTEC by subtracting a 1-hr running average (centered at ±30 min) from the TEC time series (Figueiredo et al., 2017, 2018; Tsugawa et al., 2007). We then extracted the TID parameters, such as horizontal wavelength, horizontal phase speed, period, and propagation direction, manually from the dTEC maps.

2.2. Models for the Primary and Secondary GWs From Tonga's Eruption

The Model for gravity wavE SOurce, Ray trAcing and reConstruction (MESORAC) calculates the primary GWs created from localized (in space and time) vertical updrafts of air using the Fourier-Laplace analytical fully compressible solutions (Vadas, 2013). The input parameters used in the model are determined from NOAA's Geostationary Operational Environmental Satellite (GOES-17) data. MESORAC determines the primary GWs excited by this eruption, ray traces these GWs forward in time, and reconstructs the primary GW field using the GW dissipative dispersion and polarization relations. The background atmosphere used for the ray tracing is taken from the HIAMCM simulation for 15 January 2022 without the Tonga eruption. Wave dissipation includes molecular diffusion and turbulent diffusion from saturation. The body forces and heating created by the dissipation of these primary GWs are added to the momentum and thermodynamic equations of the HIAMCM to simulate the secondary GWs from the eruption.

The HIgh Altitude Mechanistic General Circulation Model (HIAMCM) is a high-resolution whole-atmosphere model for neutral dynamics which employs a spectral dynamical core with a terrain-following hybrid vertical coordinate, a correction for non-hydrostatic dynamics, and consistent thermodynamics in the thermosphere (Becker & Vadas, 2020). The current model version has a horizontal grid spacing of 52 km and contains 280 full levels in altitude. The highest model layer is located at $z \sim 400$ km. The HIAMCM simulates GWs explicitly with an effective resolution of $\lambda_H > 200$ km. Resolved GWs are dissipated self-consistently by molecular diffusion and macro-turbulent diffusion. The large scales are nudged to Modern-Era Retrospective Analysis for Research and Applications, Version 2 (MERRA-2) reanalysis up to $z = 70$ km (Becker et al., 2022). A simple ion drag parameterization is included in the ionosphere (Becker et al., 2022b and references therein). More details about both models and their application to the Tonga eruption are contained in Vadas et al. (2023b).

2.3. 3D Ray Tracing Model

To find out if the TIDs have been generated by the primary and secondary gravity waves, we use a backward 3D ray tracing model. This ray tracing model solves the gravity wave dispersion relation including thermal diffusivity and kinematic viscosity (Vadas & Fritts, 2005). Indeed, this ray tracing model includes dissipative filtering,

Table 1
Extracted TID Parameters Over New Zealand (NZ) and Australia (AUS) on 15 January 2022 After the Tonga Volcanic Eruption

Events	Horizontal wavelength (km)	Horizontal phase speed (m/s)	Observed period (min)	Azimuth (°)	Time (UT)
NZ01	1,525 ± 137	635 ± 76	40 ± 4	214	05:10–5:30
NZ02	1,300 ± 36	551 ± 38	39 ± 3	210	05:30–06:20
NZ03	380 ± 66	358 ± 74	18 ± 2	222	06:30–07:15
NZ04	477 ± 35	361 ± 37	22 ± 2	213	08:30–09:00
AUS01	922 ± 61	375 ± 37	41 ± 3	266	06:50–07:30

critical level filtering, evanescence, frequency level filtering, and frequency changes from time-varying background winds (Vadas & Crowley, 2017; Vadas & Fritts, 2005). The input background neutral temperature, wind, and density are from the HIAMCM (Becker et al., 2022) nudged to the Modern-Era Retrospective and analysis for Research and Application-version 2 (MERRA-2) (Gelaro et al., 2017).

3. Results and Discussions

Before the volcanic eruption, two geophysical phenomena were acting on Earth and in the troposphere near the volcanic eruption. First, a high-speed stream hit the Earth's magnetic field and provoked moderate magnetic activity which led to Kp ≤ 4+ and DST index −69 nT (e.g., Gonzalez et al., 1994). However, we did not observe TIDs propagating from high latitudes over New Zealand and Australia that were associated with this moderate magnetic activity. The second geophysical phenomenon was associated with a category 1 tropical cyclone, called Cody, with winds of 95 km/hr. The cyclone Cody was located in the middle between Tonga and New Zealand. Song et al. (2019) observed MSTIDs using the dense GPS receiver network in China generated by typhoon Chan-hom in 2015. The authors observed concentric MSTIDs with horizontal phase velocities of 143 m/s and periods of 45 min. In the present study, the TIDs observed over New Zealand and Australia have different characteristics (horizontal phase speed and periods), see Table 1. Therefore, the TIDs observed after the Tonga volcanic eruption are probably associated with the volcanic eruption and are likely associated with the tsunamis generated by this explosion later in time.

Figure 2 shows a sequence of 9 snapshots of detrended TEC maps on 15 January 2022 between 06:15 and 09:03 UT. The dTEC maps have a spatial resolution of 0.2° × 0.2° in longitude and latitude. In order to minimize the lack of data in the TEC perturbations maps, the grid was smoothed by 0.6° × 0.6° in latitude and longitude.

The first wave from the Tonga eruption propagated over New Zealand at 05:15 UT, about 1 hr after the eruption. At 06:15 UT, we can only see a TID propagating southwest over New Zealand, not Australia. At 07:07 UT, we begin to observe concentric TIDs propagating over Australia (as well as New Zealand). After the large-scale TIDs propagated over New Zealand, the medium-scale TIDs also propagated over New Zealand in a similar direction as the large-scale TIDs; this occurred at 07:20 UT. After 08:00 UT, an interesting phenomenon occurred; the phase front of the TIDs observed over Australia became quasi-planar instead of circular and subdivided with one branch propagating southwestward and the other propagating westward. It suggests a superposition of several wave sources, or the wavefront became quasi-planar due to a long distance from the source. An animation of Figure 2 is available as supporting information for this paper (see Movie S1). Table 1 shows the parameters of the TIDs over New Zealand and Australia calculated manually from the dTEC maps. The first and second LSTIDs had horizontal wavelengths of 1,500 and 1,300 km, horizontal phase speeds of 635 and 550 m/s, periods of 40 and 39 min, and propagation directions of 214 and 210°. Themens et al. (2022), Zhang et al. (2022), and Wright et al. (2022) observed the first LSTIDs over New Zealand with horizontal wavelengths ranging between 1,000 and 1,500 km and radial phase speeds of 600–700 m/s. Therefore, our results are in good agreement with these studies. From Table 1, we observe that the horizontal phase speed of the TIDs over New Zealand decrease in time. Zhang et al. (2022) and Themens et al. (2022) also observed a similar behavior in the radial phase speed during the Tonga event. Despite being a different phenomenon that generated the TIDs, Tsugawa et al. (2011) observed that the phase speed of the TIDs from the Tohuku earthquake decreased in time too.

At 7:00–8:00 UT, the concentric TIDs observed over Australia overlay with the rings centered at Tonga, which would imply that these TIDs could be induced by GWs that propagated directly from the eruption. However, the phase speeds of these GWs are too fast to allow them to propagate below $z < 100$ km, since the intrinsic horizontal phase speed of a GW cannot be larger than the sound speed, which is ∼300 m/s in the lower/middle atmosphere (Vadas et al., 2019). Therefore, these GWs must have an origin in the thermosphere.

On the other hand, the phase lines of the TIDs observed over New Zealand do not overlay with the rings centered on Tonga; this is because these TIDs have a different propagation direction, with an inferred origin south of the Tonga volcanic eruption. As pointed out by Themens et al. (2022), TIDs will not always have a concentric ring structure along their trajectory. Therefore, the first TIDs observed from the Tonga event are not ideal cases to measure the radial speed (from Tonga) because the speed is affected due to wavefront curvature.

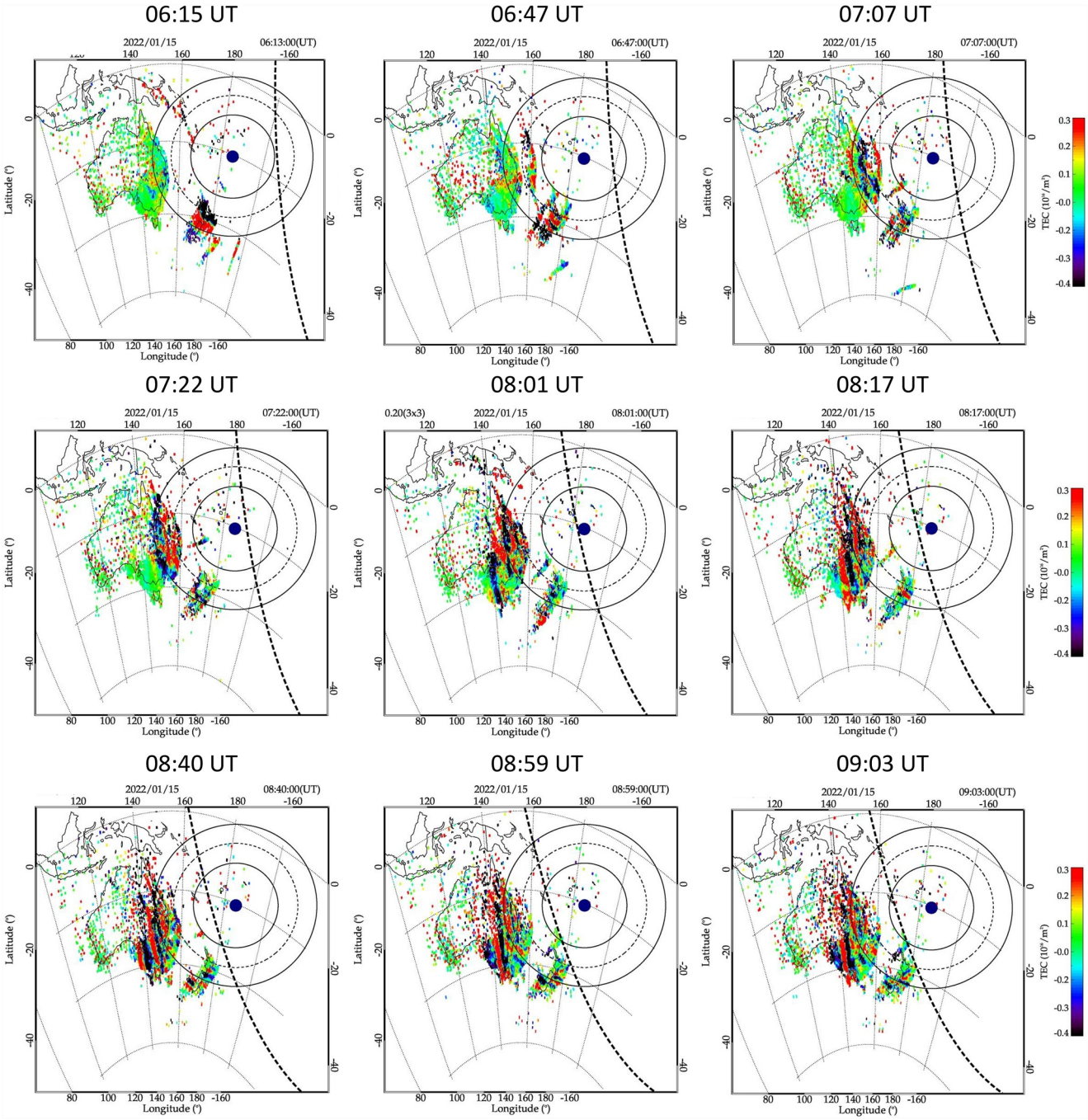

Figure 2. Detrended TEC maps over Australia and New Zealand during the Tonga volcanic eruption on 15 January 2022 from 06:13 to 09:03 UT. Alternating red and black colors indicate the TIDs generated by the Tonga eruption. The Tonga volcano is located at the blue dot. The inner to outer circles indicate the radii of 2,000, 3,000, and 4,000 km, respectively, from Tonga. The dashed black lines represent the dusk solar terminator at ∼300 km height. The color scale is in accordance with the disturbance signal, from red (positive) to black (negative).

In order to observe the temporal evolution of the TIDs in dTEC maps, we use the keogram method. A keogram is made by taking latitudinal and longitudinal cuts of each processed dTEC map, and then combining them into a time series (with a time resolution of 1 min), so that the evolution of the latitudinal and longitudinal wave components can be seen. Figure 3 shows keograms over New Zealand (a) and Australia (b) on 15 January 2022. Figure 3a shows keograms of the zonal component at 42.5°S (upper panel) and the meridional component at 172.5°E (lower panel). Figure 3b shows keograms of the zonal component at 30°S (upper panel) and the meridional component

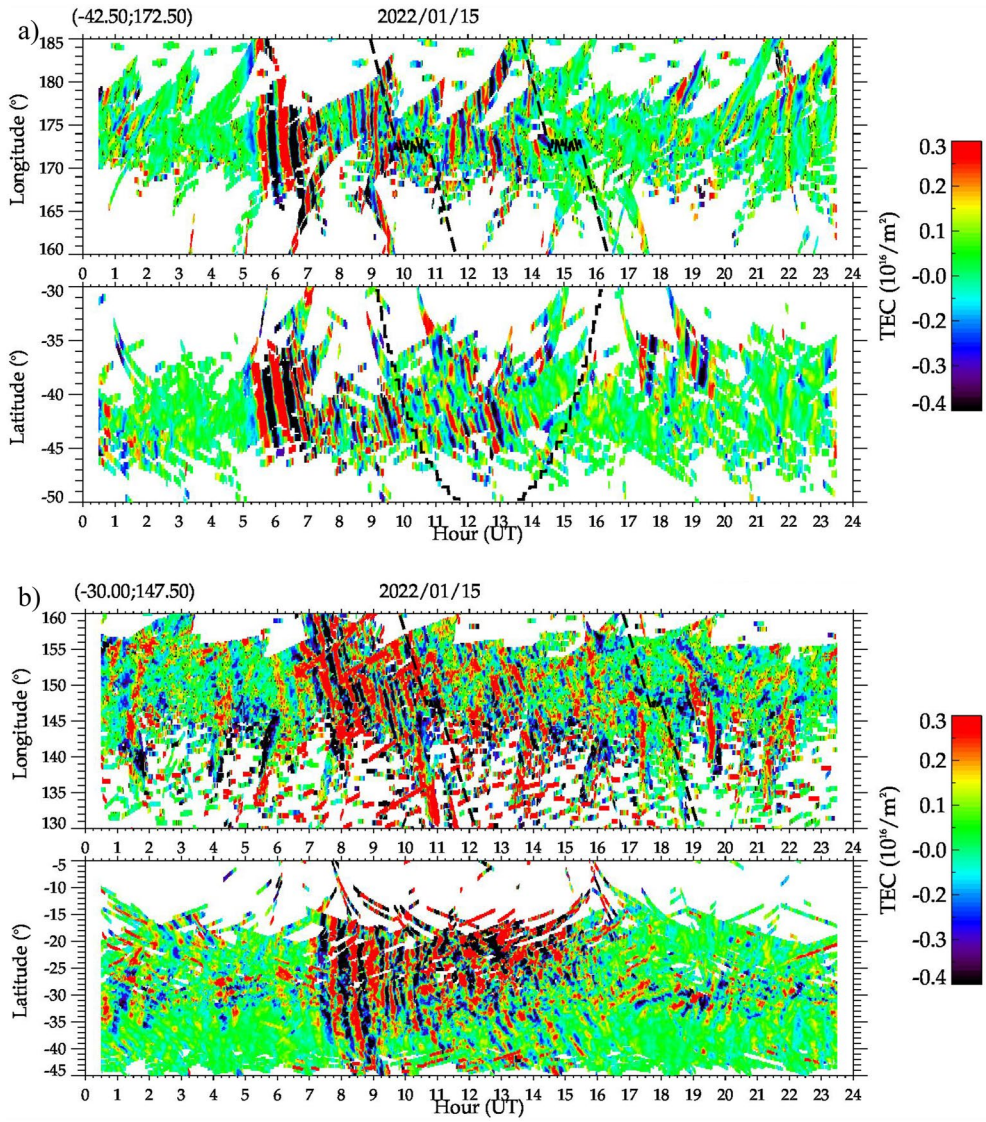

Figure 3. (a) Keograms of the zonal component at 42.5°S (upper panel) and meridional component at 172.5°E (lower panel) on 15 January 2022, over New Zealand. (b) Keograms of the zonal component at 30°S (upper panel) and meridional component at 147.5°E (lower panel) on 15 January 2022, over Australia. The TIDs are black and red variations on the keograms. The color bars are in TEC units. The dashed black lines represent the dusk and dawn solar terminator at ~300 km height. The breaks in the solar terminator dashed line are due to the low spatial and temporal resolution during the variation in longitude.

at 147.5°E (lower panel). The dashed black lines represent the dusk and dawn solar terminator at about 300 km height. We first observed the TIDs over New Zealand at 05:10 UT. The amplitudes of these first TIDs are small compared to those of subsequent TIDs. On the other hand, the first TIDs we see over Australia occur after 07:00 UT and have significantly slower phase speeds than the first TIDs we see over New Zealand (see Table 1). It is important to note that our investigation focuses on the first LSTIDs over New Zealand and Australia, despite there being more MSTIDs after 8:00 UT.

3.1. Ray Tracing

The LSTIDs observed over New Zealand are somewhat unique because they did not propagate from the epicenter of the volcanic eruption; this is because their propagation direction is somewhat different when we compare their phase lines with concentric rings centered on the Tonga eruption (see Movie S1). Therefore, this different

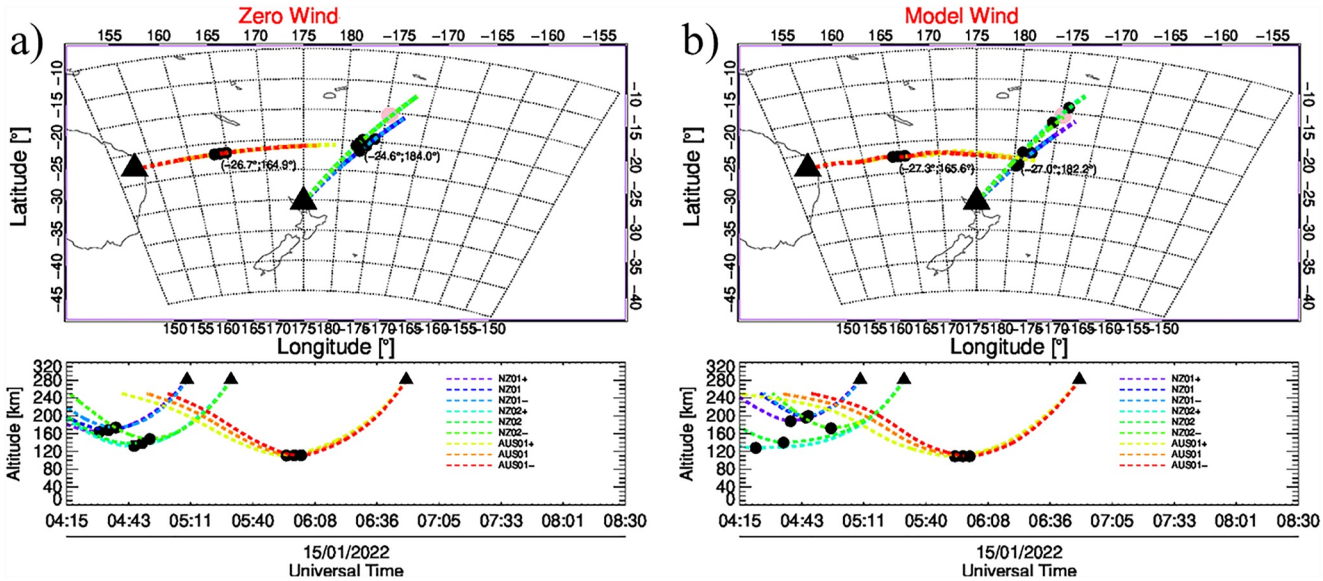

Figure 4. Reverse ray paths of the first large-scale GWs observed as LSTIDs over New Zealand and Australia as a function of longitude and latitude (upper panel) and as a function of time, and altitude (lower panel). Reverse ray tracing using (a) the HIAMCM wind nudged by large-scale MERRA-2 wind and temperature up to $z = 70$ km, and (b) zero wind. For the ray tracing, we use the GW parameters observed for the first events over New Zealand (blue and green) and Australia (red and yellow) from Table 1. The pink dot indicates the location of the Tonga volcano eruption. The black triangles and dots indicate where the ray tracing started and where the GW upward-reflected on the trace path, respectively. The colored lines show the trajectory of the individual ray path of the TIDs denoted as NZ01, NZ02, and AUS01. Note that each TID has three paths because we are considering the ray paths of the mean TID parameters (NZ/AUS), the mean parameters plus standard deviation (NZ/AUS+), and the mean parameters minus standard deviation (NZ/AUS−).

propagation direction raises an important question about the origin and excitation mechanism of these LSTIDs observed over New Zealand. To explore their origin, we assume that the TIDs were induced by large-scale GWs, and we assume that the GWs were upward-propagating when they perturbed the ionosphere. Note that the latter assumption is the only possible assumption if the GWs were created by the Tonga eruption. We then reverse ray trace the GWs using the 3D reverse ray tracing model described in Section 2.2. Figure 4 shows the ray tracing results for the first TIDs (from Table 1) observed over New Zealand (blue and green dashed lines) and Australia (red and yellow dashed lines) using the zero (a) and model wind (b). Note that each TID has three paths because we are considering the ray paths of the mean TID parameters (NZ/AUS), the mean parameters plus standard deviation (NZ/AUS+), and the mean parameters minus standard deviation (NZ/AUS−) to demonstrate the range of uncertainty as well as the sensitivity of the ray tracing model related with LSTIDs parameters and wind model. The black triangle shows the longitude, latitude, and altitude (z = 280 km) where the ray tracing began. The location of the Tonga volcano eruption is shown by the pink-filled circle. The black-filled circles on the ray paths show where and when the ray paths are reflected upward in altitude (backward in time). This upward reflection occurred because the GW horizontal phase speeds were too large to allow for the propagation of these GWs below these altitudes due to the smaller sound speed there (Vadas et al., 2019). We stop the ray tracing calculation when the TIDs reflect vertically and reach $z \geq 250$ km or reach 04:15 UT (the assumed start of the volcanic eruption), whichever comes first. Note that we reverse ray trace the TIDs for zero background wind in order to assess the magnitude of the error associated with the model wind, which is the largest component of the error.

The ray tracing results give us an important clue about the TIDs observed over NZ. We see that the GWs reverse ray traced, NZ01 and NZ02, reflected at 196 and 140 km (167 and 139 km zero wind) near the Tonga volcano, while the GWs observed over Australia reflected at 109 km (111 km zero wind) far from the volcanic eruption. Because neither of these GWs could have been created below $z < 100$ km, neither of these GWs could have been "primary" GWs created directly by the eruption. Because the dissipation of primary GWs from Tonga created secondary GWs with horizontal phase speeds of 100–600 m/s (Vadas et al., 2023a), our ray trace results suggest that these TIDs were induced by secondary gravity waves generated by the breaking/dissipation of primary gravity waves created by the Tonga volcanic eruption. It is important to note that the GWs that induced the TIDs could have been created anywhere along the ray trace paths dashed lines in Figure 4.

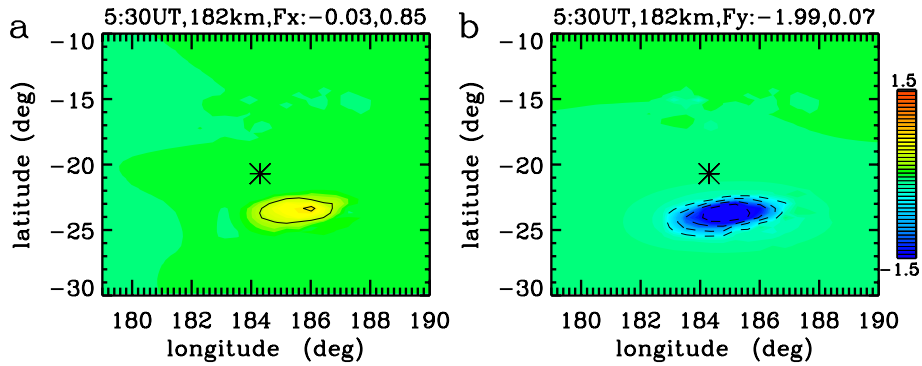

Figure 5. Vertical flux of zonal (a) and meridional (b) momentum flux (i.e., zonal and meridional local body forces, respectively) at 5:30 UT at $z = 182$ km altitude. The color indicates the body force amplitudes (in m/s^2). The black asterisks indicate the position of the Tonga eruption.

Regarding the uncertainty and sensitivity of the ray tracing model, we note that the LSTIDs (NZ/AUS+) longer horizontal wavelength, period, and faster horizontal phase speed result in its probable propagation closer to the Tonga volcano eruption. Moreover, the ray tracing calculation with wind background causes the paths to lengthen and move closer to the site of the Tonga volcano eruption. Additionally, the reflection points alter their position even further when compared with zero wind. Similarly, the uncertainty and sensitivity of ray tracing, with both zero and model background wind, to MSTIDs NZ03 and NZ04 were discussed in Appendix A.

3.2. Numerical Simulation of Primary and Secondary Gravity Waves

During the Tonga volcano eruption, many massive updrafts were created which extended up to $z = 58$ km altitude (Carr et al., 2022). Here, we use results from a recent modeling effort to explain the physical mechanism that created the upward-propagating large-scale GWs that reached the ionosphere over New Zealand and Australia from the Tonga eruption.

Figure 5 shows the zonal (a) and meridional (b) component body forces at 182 km altitude and at 5:30 UT created by the dissipation of primary GWs at 22.5–25.5°S; 183.0–187.0°E. A large-amplitude body force is created southeast-south of the Tonga eruption. Note that the distance between the eruption and this body force is ∼350–600 km. The amplitude of the zonal component of the body force is weaker than that of the meridional component of body force. We now compare this result with the backward ray tracing result shown in Figure 4. We can observe that the first LSTID's backward path over New Zealand is close to the body force region, indicating accurate ray tracing calculations and the probable source is from the Tonga volcano eruption. On the other hand, there are two potential explanations for the disagreement between the backward ray tracing of the LSTID from Australia and the body force region generated by the Tonga Explosion: inaccurate background parameters such as temperature and wind, or the limitation of the body forces/heatings computed by MESORAC by adjusting the turbulent diffusion parameter in the saturation scheme as described by Vadas et al. (2023b).

Next, we show the results from the MESORAC/HIAMCM model study. Figure 6 shows 2D maps of the secondary GWs in the vertical neutral wind (w) generated by the HIAMCM model with MESORAC inputs every 30 min from 5:30 UT to 8:00 UT on 15th January over an area ranging from 0 to 50°S and 120–240°E. Our goal is to analyze the first LSTIDs over New Zealand and Australia and discuss the physical mechanism based on secondary gravity waves. We do not discuss the simulation results after 8:00 UT since these MSTIDs could be generated by various sources, such as tsunamis, acoustic gravity waves, and secondary gravity waves.

In Figure 6, the first secondary GW generated by the HIAMCM propagated over New Zealand at 05:30–05:45 UT with horizontal wavelength, horizontal phase speed, period, and azimuth of 1,234 km, 447 m/s, 46 min, 205°, respectively. The horizontal wavelength, period, and azimuth of this GW agree reasonably well with that observed in the TEC (see Table 1); however, the propagation speed of this GW is slower than the observed speed.

It is important to note from Figure 6 that the secondary GWs mainly propagate northward and southward instead of having equal amplitudes in all directions. This is the typical radiation pattern for secondary GWs excited by a horizontal

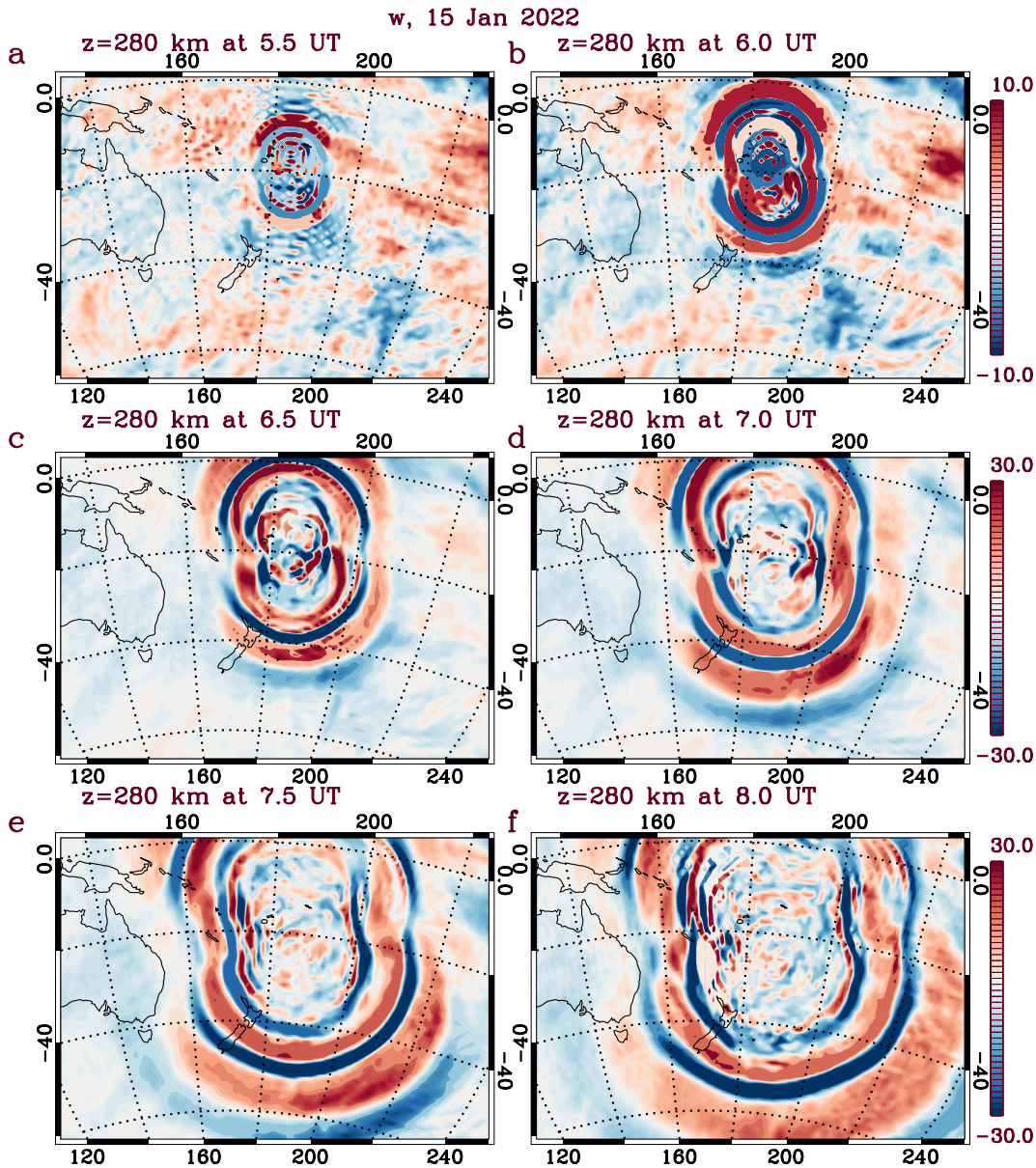

Figure 6. 2D maps of the secondary GWs as seen in the vertical neutral wind at 280 km altitude as simulated by the HIAMCM on 15th January, between 05:30 and 08:00 UT every 0.5 hr. The colorbar shows the amplitude of the vertical velocity (in m/s).

body force (i.e., local horizontal acceleration) (Vadas et al., 2003, 2018). This body force accelerates the background flow in the direction of propagation of the primary GWs. The fluid reacts by producing two counter-rotating cells (Vadas & Liu, 2009) by generating secondary GWs that propagate in all directions except perpendicular to the body force direction (Vadas et al., 2003, 2018). These secondary GWs propagate upward, downward, forward, and backward from the body force. For the HIAMCM results shown in Figure 6d, there are some faint GWs over Australia at 7:00 UT propagating to the southwest, west, and northwest; however, those GWs were slower than those that propagated first to New Zealand. Comparing the HIAMCM results with the dTEC maps in Figure 2, we see that the propagation direction and horizontal wavelengths of the HIAMCM GW are in agreement with that of the TIDs. Furthermore, the wavefront of the first LSTIDs of the HIAMCM over Australia appears quasi-planar, as seen in Figure 2. The HIAMCM results show that the observed LSTIDs in Figure 2 after 7:00 UT are probably due to a superposition of LSTIDs from secondary gravity waves generated by north and south body forces. Therefore, the body force mechanism is an important physical mechanism for upward GWs in the thermosphere/ionosphere, as we observed over New Zealand and Australia during the Tonga event.

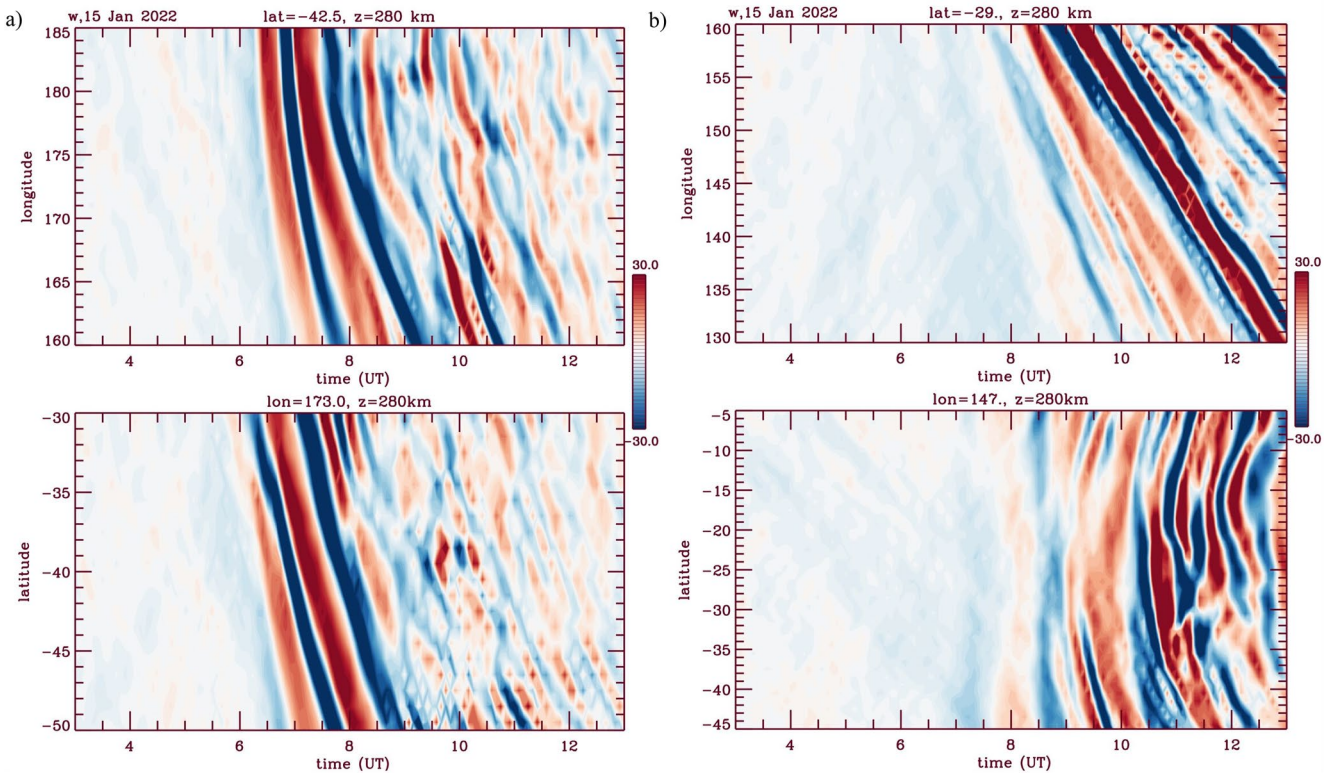

Figure 7. (a) Keograms of the vertical velocity (colors) as simulated by the HIAMCM at −42.5°N (upper panel) and at 173°E (lower panel) on 15 January 2022, over New Zealand. (b) Keograms of the vertical velocity as simulated by the HIAMCM at −29°N (upper panel) and at 147°E (lower panel) on 15 January 2022, over Australia. The blue and red variations indicate the GW perturbations in the thermosphere. The color bars are the vertical wind perturbation amplitude (m/s).

Figure 7 shows keograms of the vertical velocity from the HIAMCM over New Zealand (a) and Australia (b) on 15 January 2022 from 3:00 UT to 13:00 UT. Figure 7a shows keograms at −42.5°N (upper panel) and at 173.0°E (lower panel). Figure 3b shows keograms at −29°N (upper panel) and at 147.0°E (lower panel). The first secondary GWs propagate over New Zealand at ∼05:30 UT. On the other hand, the first secondary GWs propagate over Australia at 07:30 UT. Both of these GWs are quite faint.

In order to compare the dTEC maps observed on 15 January 2022, with the secondary GWs simulated by HIAMCM, we use the SAMI3 to see how the ionosphere response to the secondary GWs in dTEC maps. The SAMI3 is a 3D global physics-based model of the ionosphere/plasmasphere system. It is based on the original SAMI2 model (Huba et al., 2000). SAMI3 models the plasma and chemical evolution of seven ion species (H^+, He^+, N^+, O^+, N_2, NO^+, and O_2^+). Besides that, the temperature equation is solved for three ion species (H^+, He^+, and O^+) and for the electrons. Further details on the model have been discussed in previous papers (e.g., Huba & Joyce, 2010; Huba & Liu, 2020; Huba et al., 2023).

Figures 8a and 8c show dTEC maps with TIDs signatures using GNSS receivers, and Figures 8b and 8d show the TIDs induced via ion-neutral coupling from the secondary GWs simulated by SAMI3. For the SAMI3 results, the secondary GWs are inputted from the HIAMCM for the Tonga eruption (Vadas et al., 2023a). The simulation result (Figures 8b and 8d) shows that the first TID arrived over NZ (at 5:44 UT) with a horizontal wavelength of 1,234 km, a horizontal phase speed of 447 m/s, a period of 46 min, and an amplitude of ±1.0–1.5 TECU. When we compare the simulations with observation results, the morphology, horizontal wavelength, and observational period of the first TIDs simulated by SAMI 3 agree well with the TIDs observed by the GNSS receivers. However, the amplitudes of the SAMI3 TIDs are ∼1TECU larger than the amplitudes of the observed TIDs. In addition, the SAMI3 TIDs are delayed by 30 min with respect to the GNSS observations. This is consistent with the results from Vadas et al. (2023a), who found that the HIAMCM GWs were delayed by the ICON-MIGHTI winds by ∼30 min. They postulated that this delay occurred because the turbulent diffusion coefficient was somewhat too large in MESORAC in order to keep the HIAMCM Tonga simulation from becoming unstable.

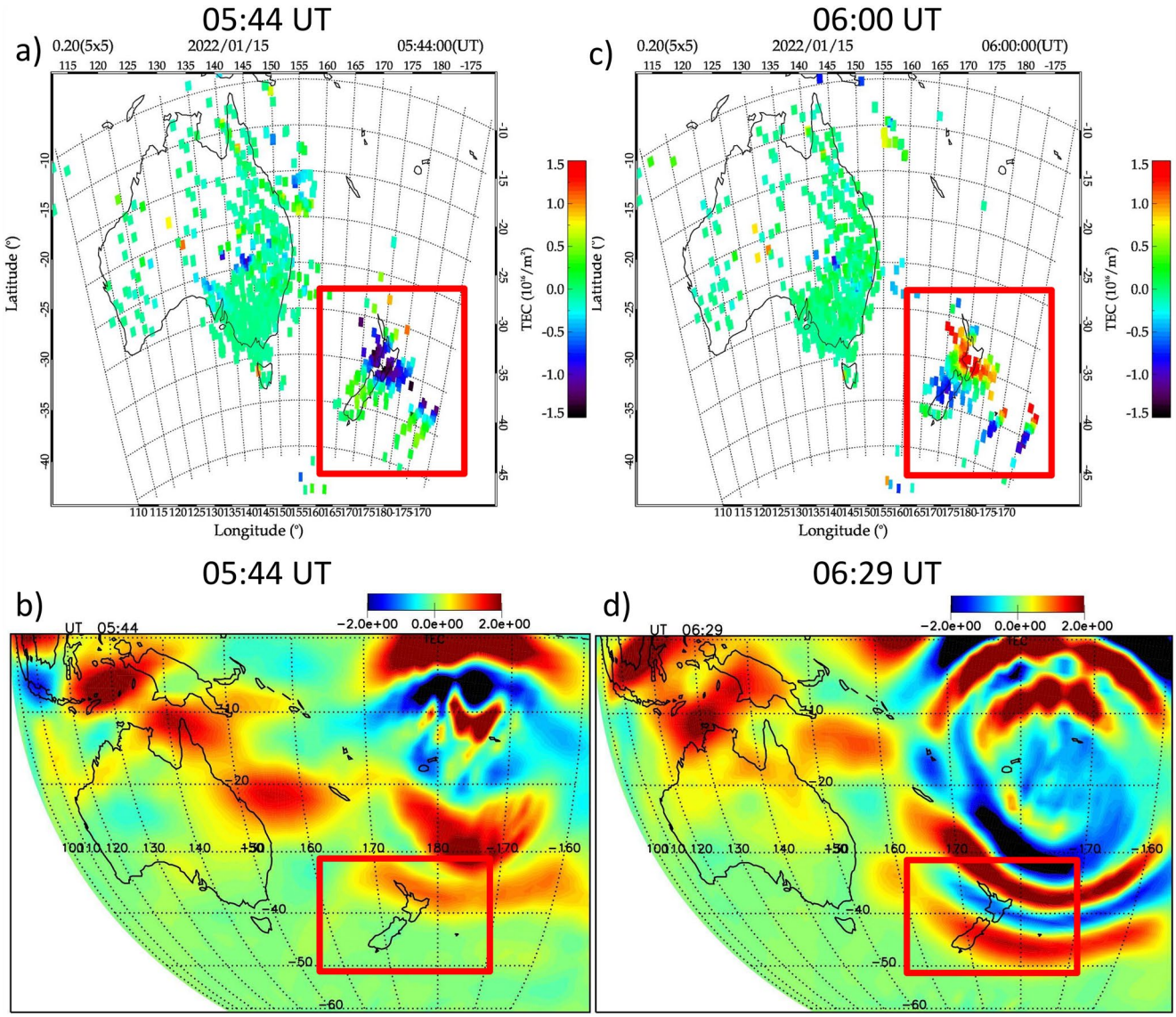

Figure 8. Figure 8 shows 2D dTEC maps observed using GNSS receivers (a and c) and modeling by SAMI3 (b and d) on 15 January 2022, between 05:44 and 06:29 UT, respectively. The red rectangles indicate the region where the TIDs observed and simulated were considered.

On the other hand, the TIDs from Australia arrived about 2 hr after the TIDs over New Zealand, as shown in Figure 2. We do see slightly elevated dTEC values in SAMI 3 over Australia at 5:44 and 6:29 UT in Figures 8b and 8d. However, they do not appear to be TIDs from Tonga. The result that showed TIDs were apparent ∼2 hr later in Australia than in New Zealand was first noticed by Themens et al. (2022).

Finally, the most striking feature of this event is the physical mechanism that generates the TIDs in the ionosphere. Lamb waves from the Tonga event traveled horizontally in the troposphere, without dissipation. This wave had a horizontal speed of about 318 m/s in the stratosphere (Wright et al., 2022). These waves were concentrated in the troposphere because the wave energy densities decrease exponentially with altitude (Gossard & Hooke, 1975). Nishida et al. (2013) investigated the Lamb wave in the Earth's atmosphere and found that Lamb wave horizontal oscillations can force or trigger GWs in the thermosphere similar to a forced oscillator mechanism. Such GWs can then propagate outward and upward. A condition of this mechanism is that the horizontal wavelength and period of the forced GW must be the same as that of the Lamb wave. Therefore, the LSTIDs observed over New Zealand and Australia are not Lamb waves, primary gravity waves, or acoustic waves in the ionosphere for the following reasons. The reason they cannot be Lamb waves is that the horizontal phase speed of ∼600 m/s. Also, since GWs

cannot propagate faster than 90% of the sound speed in the lower and middle atmosphere, these waves cannot be primary gravity waves from the Tonga eruption. The reason they cannot be acoustic waves is that the observed period (~40 min) is much greater than the buoyancy period (~9–12 min in the F region); therefore, they can only be a gravity wave (since acoustic waves have periods < buoyancy period). Taking into consideration all these points, we conclude that the LSTIDs observed over New Zealand and Australia are induced by secondary gravity waves created by the multi-step vertical coupling of the primary GWs excited by the Tonga eruption.

4. Conclusions

The Tonga volcanic eruption generated several kinds of waves in the atmosphere, as shown by Wright et al. (2022). In this current study, we investigated TIDs in the F region ionosphere using detrended GPS-GLONASS/TEC data. We found that the observed TIDs have horizontal wavelengths ranging from 350 to 1,500 km, horizontal phase speed between 350 and 650 m/s, and observed periods of 18–40 min. We backward ray traced the first TID observed over New Zealand and Australia, and found that these TIDs could not have propagated directly from the eruption. Furthermore, sensitivity studies about the ray tracing model results were also conducted. The sensitivity analysis revealed that the HIAMCM model's wind patterns cause elongation in the ray paths, bringing it closer to the eruption of the Tonga volcano.

In order to investigate the physical mechanism behind the generation of these LSTIDs, we modeled the primary GWs excited by the Tonga eruption and estimated the body forces created during the dissipation using the MESORAC model. We added these local body forces into the nudged HIAMCM, which then generated a rich spectrum of secondary gravity waves. The HIAMCM results were inputted into SAMI3, which generated TIDs.

Regarding the sources of LSTIDs, the MESORAC, HIAMCM, and ray trace results showed that the secondary gravity waves over New Zealand did not originate directly from the volcano epicenter; instead, they originated from a local body force created 436 km southeast of Tonga volcano. From the SAMI3, the simulated LSTIDs agree well with the observed LSTIDs, which emphasizes the fact that all the simulations used in this study are within a very good precision, hence their ability to relate the entire coupling process that arose from the eruption. The timing of the wave occurrence was only delayed by ~20–30 min in the SAMI3 results. The TIDs were observed 2–3 hr later over Australia than over New Zealand, which agrees reasonably well with model results.

Therefore, the physical mechanism that explains the asymmetry in the TIDs wavefronts generated by secondary gravity waves is (a) the body force mechanism and (b) GW propagation perpendicular to the magnetic field does not induce TIDs (Vadas et al., 2023a).

Appendix A

Ray tracing results of the MSTIDs NZ03 and NZ04 are presented in Figure A1. For each event, the mean MSTIDs parameters (NZ03, NZ04), the mean TIDs parameters plus the standard deviation (NZ03+, NZ04+), and the mean TIDs parameters minus the standard deviation (NZ03−, NZ04−) are presented. In panels (a) and (b), the ray tracing zero and model wind result of the MSTIDs of NZ03+, NZ03, NZ03− and NZ04+, NZ04, NZ04−. The upper panel presents the trajectory of the TIDs in longitude and latitude. The black dots, black triangles, and light pink dots indicate the location where the reflection occurred, the location where the ray tracing began, and the location of the Tonga volcano eruption, respectively. In the lower panel, the variation of the ray path as a function of time and altitude is presented.

The purpose of this plot is to test the response of the ray tracing model to the uncertainty in the wind and the MSTIDs parameters when studying the propagation of the observed MSTIDs. Considering the standard deviation, it can be clearly seen the ray path did not vary significantly, indicating that variation in the model is mainly due to the wind as mentioned earlier. A similar test was conducted by Nyassor et al. (2022) to see how their ray tracing model responded when using the zero and model wind employing the propagation error technique (Bevington & Robinson, 2003). Even though they were studying small-scale GWs, they found that the error due to wind was less than 10% of the expected values and mainly due to the wind as shown in the present study. This error affects the trajectory of the wave understudy both in time and space. The result shown in this current study further demonstrated that the ray tracing model is estimating the ray paths at a good precision.

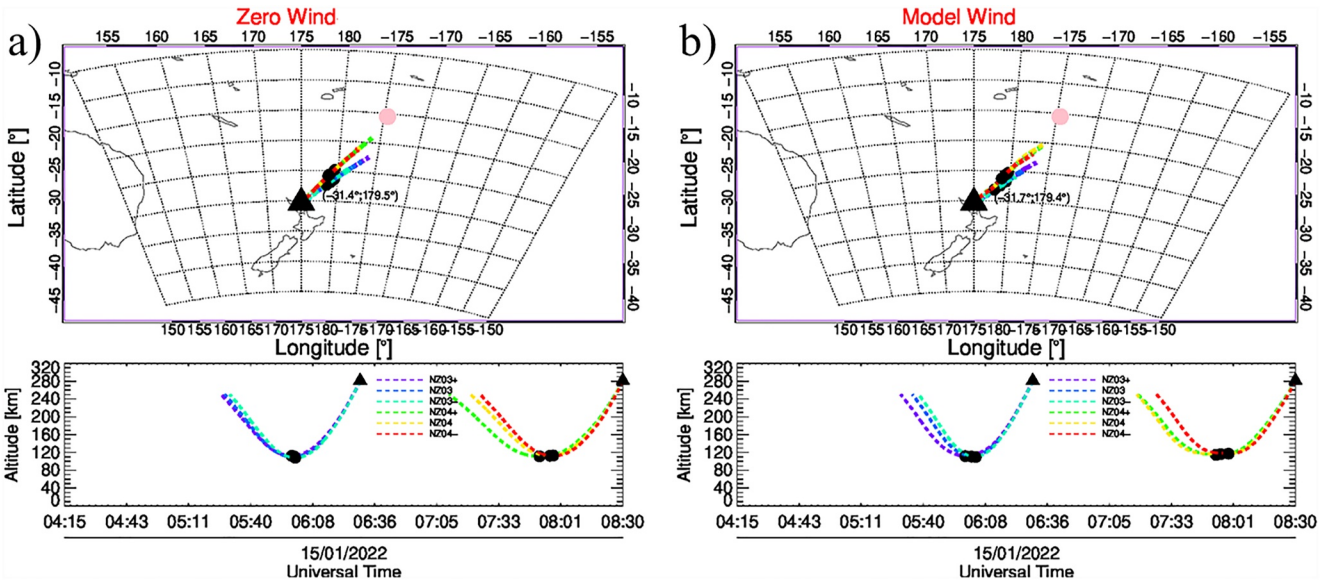

Figure A1. Backward ray paths of the medium-scale TIDs observed over New Zealand as a function of longitude and latitude (upper panel), and as a function of time and altitude (lower panel). Reverse ray tracing was run in both zero (a) and model (b) wind mode. For the ray tracing, we use the MSTIDs parameters observed over New Zealand from Table 1. The light pink dot indicates the location of the Tonga volcano eruption. The black triangles and dots indicate where the ray tracing started and where the GW upward reflected on the trace path, respectively. The colored lines correspond to the individual ray path of the waves (NZ03 and NZ04). Note that each LSTID has three paths because we are considering the ray paths of the mean LSTID parameters (NZ), the mean parameters plus standard deviation (NZ+), and the mean parameters minus standard deviation (NZ−).

Data Availability Statement

The Global Navigation Satellite System (GNSS) RINEX files used in this work are available from the Geological Hazard information for New Zealand (https://www.geonet.org.nz/data/types/geodetic) and the Geoscience Australia GNSS data archive (https://www.ga.gov.au/scientific-topics/positioning-navigation/geodesy/gnss-networks). The model data shown in this paper will be available in English at the time of publication at https://www.cora.nwra.com/vadas/Vadas-etal-JGR-2023-TongaTEC-files/.

Acknowledgments

C. A. O. B., Figueiredo thanks Fundação de Amparo à Pesquisa do Estado de São Paulo (FAPESP) by Grants 2018/09066–8 and 2019/22548-4. Also, he thanks Fundação de Apoio a Pesquisa do Estado da Paraíba (FAPESq). Thanks to the Brazilian Ministry of Science, Technology and Innovation (MCTI) and the Brazilian Space Agency (AEB) who supported the present work under the Grant PO 20VB.0009. SLV and EB were supported by NASA Grants 80NSSC19K0836, 80NSSC20K0628, and 80NSSC22K0174. SLV was also supported by NSF Grants AGS-1822867 and AGS-1832988. EB was additionally supported by the Leibniz Institute of Atmospheric Physics at the University of Rostock (IAP), which partly provided the HPC facility used for this study. KB was supported by NASA Grant 80NSSC19K0836. The author would like to thank Joe Huba for the SAMI 3 data.

References

Astafyeva, E. (2019). Ionospheric detection of natural hazards. *Reviews of Geophysics*, *57*(4), 1265–1288. https://doi.org/10.1029/2019RG000668

Astafyeva, E., Maletckii, B., Mikesell, T. D., Munaibari, E., Ravanelli, M., Coisson, P., et al. (2022). The 15 January 2022 Hunga Tonga eruption history as inferred from ionospheric observations. *Geophysical Research Letters*, *49*(10), e2022GL098827. https://doi.org/10.1029/2022GL098827

Becker, E., Goncharenko, L., Harvey, V. L., & Vadas, S. L. (2022b). Multi-step vertical coupling during the January 2017 sudden stratospheric warming. *Journal of Geophysical Research: Space Physics*, *127*(12), e2022JA030866. https://doi.org/10.1029/2022JA030866

Becker, E., & Vadas, S. L. (2020). Explicit global simulation of gravity waves in the thermosphere. *Journal of Geophysical Research: Space Physics*, *125*(10), e2020JA028034. https://doi.org/10.1029/2020JA028034

Becker, E., Vadas, S. L., Bossert, K., Harvey, V. L., Z ̈ulicke, C., & Hoffmann, L. (2022). A high-resolution whole-atmosphere model with resolved gravity waves and specified large scale dynamics in the troposphere and stratosphere. *Journal of Geophysical Research: Space Physics*, *127*(2), e2021JD035018. https://doi.org/10.1029/2021JD035018

Bevington, P. R., & Robinson, D. K. (2003). *Data reduction and error analysis for the physical sciences* (3rd ed.). McGraw-Hill.

Carr, J. L., Horváth, Á., Wu, D. L., & Friberg, M. D. (2022). Stereo plume height and motion retrievals for the record-setting Hunga Tonga-Hunga Ha'apai eruption of 15 January 2022. *Geophysical Research Letters*, *49*(9), e2022GL098131. https://doi.org/10.1029/2022GL098131

Figueiredo, C. A. O. B., Takahashi, H., Wrasse, C. M., Otsuka, Y., Shiokawa, K., & Barros, D. (2018). Medium-scale traveling ionospheric disturbances observed by detrended total electron content maps over Brazil. *Journal of Geophysical Research: Space Physics*, *123*(3), 2215–2227. https://doi.org/10.1002/2017JA025021

Figueiredo, C. A. O. B., Wrasse, C. M., Takahashi, H., Otsuka, Y., Shiokawa, K., & Barros, D. (2017). Large-scale traveling ionospheric disturbances observed by GPS dTEC maps over North and South America on Saint Patrick's Day storm in 2015. *Journal of Geophysical Research: Space Physics*, *122*(4), 4755–4763. https://doi.org/10.1002/2016JA023417

Gelaro, R., McCarty, W., Suárez, M. J., Todling, R., Molod, A., Takacs, L., et al. (2017). The modern-era retrospective analysis for research and, version 2 (MERRA-2). *Journal of Climate*, *30*(14), 5419–5454. https://doi.org/10.1175/JCLI-D-16-0758.1

Gonzalez, W. D., Joselyn, J. A., Kamide, Y., Kroehl, H. W., Rostoker, G., Tsurutani, B. T., & Vasyliunas, V. M. (1994). What is a geomagnetic storm? *Journal of Geophysical Research*, *99*(A4), 5771–5792. https://doi.org/10.1029/93JA02867

Gossard, E., & Hooke, W. (1975). *Waves in the atmosphere*. Elsevier.

Gusman, A. R., & Roger, J. (2022). Hunga Tonga—Hunga Ha'apai volcano-induced sea level oscillations and tsunami simulations. *GNS Science Webpage*. https://doi.org/10.21420/DYKJRK41

Huba, J. D., Becker, E., & Vadas, S. L. (2023). Simulation study of the 15 January 2022 Tonga event: Development of super equatorial plasma bubbles. *Geophysical Research Letters*, *50*(1), e2022GL101185. https://doi.org/10.1029/2022GL101185

Huba, J. D., & Joyce, G. (2010). Global modeling of equatorial plasma bubbles. *Geophysical Research Letters*, *37*(17), L17104. https://doi.org/10.1029/2010GL044281

Huba, J. D., Joyce, G., & Fedder, J. A. (2000). Sami2 is another model of the ionosphere (SAMI2): A new low-latitude ionosphere model. *Journal of Geophysical Research*, *105*(A10), 23035–23053. https://doi.org/10.1029/2000JA000035

Huba, J. D., & Liu, H.-L. (2020). Global modeling of equatorial spread F with SAMI3/WACCM-X. *Geophysical Research Letters*, *47*(14), e2020GL088258. https://doi.org/10.1029/2020GL088258

Igakashi, K., Kainuma, S., Nishimuta, I., Okamoto, S., Kuroiwa, H., Tanaka, T., & Ogawa, T. (1993). Ionospheric and atmospheric disturbances around Japan caused by the eruption of Mount Pinatubo on 15 June 1991. *Journal of Atmospheric and Terrestrial Physics*, *56*(9), 1227–1234.

Lin, J.-T., Rajesh, P. K., Lin, C. C. H., Chou, M.-Y., Liu, J.-Y., Yue, J., et al. (2022). Rapid conjugate appearance of the giant ionospheric Lamb wave signatures in the northern hemisphere after Hunga-Tonga volcano eruptions. *Geophysical Research Letters*, *49*(8), e2022GL098222. https://doi.org/10.1029/2022GL098222

Nishida, K., Kobayashi, N., & Fukao, Y. (2013). Background Lamb waves in the Earth's atmosphere. *Geophysical Journal International*, *196*(1), 312–316. https://doi.org/10.1093/gji/ggt413

Nyassor, P. K., Wrasse, C. M., Paulino, I., São Sabbas, E. F. M. T., Bageston, J. V., Naccarato, K. P., et al. (2022). Sources of concentric gravity waves generated by a moving mesoscale convective system in southern Brazil. *Atmospheric Chemistry and Physics*, *22*(23), 15153–15177. https://doi.org/10.5194/acp-22-15153-2022

Poli, P., & Shapiro, M. (2022). Rapid characterization of large volcanic eruptions: Measuring the impulse of the Hunga Tonga explosion from teleseismic waves. *Geophysical Research Letters V.*, *49*(8), e2022GL098123. https://doi.org/10.1029/2022GL098123

Song, Q., Ding, F., Zhang, X., Liu, H., Mao, T., Zhao, X., & Wang, Y. (2019). Medium-scale traveling ionospheric disturbances induced by Typhoon Chan-hom over China. *Journal of Geophysical Research: Space Physics*, *124*(3), 2223–2237. https://doi.org/10.1029/2018JA026152

Themens, D. R., Watson, C., Žagar, N., Vasylkevych, S., Elvidge, S., McCaffrey, A., et al. (2022). Global propagation of ionospheric disturbances associated with the 2022 Tonga volcanic eruption. *Geophysical Research Letters*, *49*(7), e2022GL098158. https://doi.org/10.1029/2022GL098158

Tsugawa, T., Otsuka, Y., Coster, A. J., & Saito, A. (2007). Medium-scale traveling ionospheric disturbances detected with dense and wide TEC maps over North America. *Geophysical Research Letters*, *34*(22), L22101. https://doi.org/10.1029/2007GL031663

Tsugawa, T., Saito, A., Otsuka, Y., Nishioka, M., Maruyama, T., Kato, H., et al. (2011). Ionospheric disturbances detected by GPS total electron content observation after the 2011 off the Pacific coast of Tohoku Earthquake. *Earth Planets and Space*, *63*(7), 66–879. https://doi.org/10.5047/eps.2011.06.035

Vadas, S. L. (2013). Compressible f-plane solutions to body forces, heatings, and coolings and application to the primary and secondary gravity waves generated by a deep convective plume. *Journal of Geophysical Research: Space Physics*, *118*(5), 2377–2397. https://doi.org/10.1002/jgra.50163

Vadas, S. L., Becker, E., Figueiredo, C., Bossert, K., Harding, B. J., & Gasque, L. C. (2023a). Primary and secondary gravity waves and large-scale wind changes generated by the Tonga volcanic eruption on 15 January 2022: Modeling and comparison with ICON-MIGHTI winds. *Journal of Geophysical Research: Space Physics*, *128*(2), e2022JA031138. https://doi.org/10.1029/2022JA031138

Vadas, S. L., & Crowley, G. (2017). Neutral wind and density perturbations in the thermosphere created by gravity waves observed by the TIDDBIT sounder. *Journal of Geophysical Research: Space Physics*, *122*(6), 6652–6678. https://doi.org/10.1002/2016JA023828

Vadas, S. L., Figueiredo, C., Becker, E., Huba, J. D., Themens, D. R., Hindley, N. P., et al. (2023b). Traveling ionospheric disturbances induced by the secondary gravity waves from the Tonga eruption on 15 January 2022: Modeling with MESORAC-HIAMCM-SAMI3 and comparison with GPS/TEC and ionosonde data. *Journal of Geophysical Research: Space Physics*, *128*(6), e2023JA031408. https://doi.org/10.1029/2023JA031408

Vadas, S. L., & Fritts, D. C. (2005). Thermospheric responses to gravity waves: Influences of increasing viscosity and thermal diffusivity. *Journal of Geophysical Research*, *110*(D15), D15103. https://doi.org/10.1029/2004JD005574

Vadas, S. L., Fritts, D. C., & Alexander, M. J. (2003). Mechanism for the generation of secondary waves in wave breaking regions. *Journal of the Atmospheric Sciences*, *60*(1), 194–214. https://doi.org/10.1175/1520-0469(2003)060<0194:mftgos>2.0.co;2

Vadas, S. L., & Liu, H. L. (2009). Generation of large-scale gravity waves and neutral winds in the thermosphere from the dissipation of convectively generated gravity waves. *Journal of Geophysical Research*, *114*(A10), A10310. https://doi.org/10.1029/2009ja014108

Vadas, S. L., Xu, S., Yue, J., Bossert, K., Becker, E., & Baumgarten, G. (2019). Characteristics of the quiet-time hotspot gravity waves observed by GOCE over the Southern Andes on 5 July 2010. *Journal of Geophysical Research: Space Physics*, *124*(8), 7034–7061. https://doi.org/10.1029/2019JA026693

Vadas, S. L., Zhao, J., Chu, X., & Becker, E. (2018). The excitation of secondary gravity waves from local body forces: Theory and observation. *Journal of Geophysical Research: Atmospheres*, *123*(17), 9296–9325. https://doi.org/10.1029/2017JD027970

Wright, C., Hindley, N., Alexander, M. J., Barlow, M., Hoffmann, L., Mitchell, C., et al. (2022). Surface-to-space atmospheric waves from Hunga Tonga-Hunga ha´apai eruption. *Earth and Space Science Open Archive*, *703 23*, 2269–2277. https://doi.org/10.1002/essoar.10510674.2

Zhang, S.-R., Vierinen, J., Aa, E., Goncharenko, L., Erickson, P., Rideout, W., et al. (2022). Tonga volcanic eruption induced global propagation of ionospheric disturbances via lamb waves. *Frontiers in Astronomy and Space Sciences*, *9*, 871275. https://doi.org/10.3389/fspas.2022.871275